Solenoid-free current drive via ECRH in EXL-50 spherical torus plasmas

PAPER • OPEN ACCESS

Solenoid-free current drive via ECRH in EXL-50 spherical torus plasmas

To cite this article: Yuejiang Shi *et al* 2022 *Nucl. Fusion* **62** 086047

OPEN ACCESS
IOP Publishing | International Atomic Energy Agency Nuclear Fusion
Nucl. Fusion **62** (2022) 086047 (10pp) https://doi.org/10.1088/1741-4326/ac71b6

Solenoid-free current drive via ECRH in EXL-50 spherical torus plasmas

Yuejiang Shi*, Bing Liu*, Shaodong Song, Yunyang Song, Xianming Song, Bowei Tong, Shikui Cheng, Wenjun Liu, Mingyuan Wang, Tiantian Sun, Dong Guo, Songjian Li, Yingying Li, Bin Chen, Xiang Gu, Jianqing Cai, Di Luo, Debabrata Banerjee, Xin Zhao, Yuanming Yang, Wenwu Luo, Peihai Zhou, Yu Wang, Akio Ishida, Takashi Maekawa, Minsheng Liu, Baoshan Yuan, Y.-K. Martin Peng* and the EXL-50 Team

Hebei Key Laboratory of Compact Fusion, Langfang 065001, China
Enn Science and Technology Development Co., Ltd, Langfang 065001, China

E-mail: shiyuejiang@enn.cn, liubingw@enn.cn and pengyuankai@enn.cn

Received 22 December 2021, revised 11 May 2022
Accepted for publication 20 May 2022
Published 7 July 2022

Abstract

As a new spherical tokamak designed to simplify the engineering requirements of a possible future fusion power source, the EXL-50 experiment features a low aspect ratio vacuum vessel (VV), encircling a central post assembly containing the toroidal field coil conductors without a central solenoid. Multiple electron cyclotron resonance heating (ECRH) resonances are located within the VV to improve current drive effectiveness. Copious energetic electrons are produced and measured with hard x-ray detectors, carry the bulk of the plasma current ranging from 50–150 kA, which is maintained for more than 1 s duration. It is observed that over one ampere current can be sustained per watt of ECRH power issued from the 28 GHz gyrotrons. The plasma current reaches $I_p > 80$ kA for high density ($>5 \times 10^{18}$ m^{-2}) discharge with 150 kW ECRH. An analysis was carried out combining reconstructed multi-fluid equilibrium, guiding-center orbits of energetic electrons, and resonant heating mechanisms. It is verified that in EXL-50 a broadly distributed current of energetic electrons creates a smaller closed magnetic-flux surface of low aspect ratio that in turn confines the thermal plasma electrons and ions and participate in maintaining the equilibrium force balance.

Keywords: spherical torus, solenoid-free current drive, ECRH

(Some figures may appear in colour only in the online journal)

1. Introduction

Great progress has been achieved in magnetic confinement fusion research based on the tokamak since 50 years ago when the first stable high temperature plasma was observed in the T-3 tokamak [1–3]. The tokamak has been the most investigated and furthest advanced configuration among the magnetic confinement fusion systems. More recently, the spherical tokamak (ST) concept of aspect ratios around 1.5 [4, 5] has been experimentally (START [6], NSTX [7], MAST [8] and Globus-M [9]) tested to realize a substantially higher plasma beta compared to the tokamak of aspect ratios around 3, and is an attractive candidate for realizing a relatively compact fusion reactor. In this article, the special torus (ST) indicates the ST.

The tokamak plasma current is required to ensure a high plasma confinement capability to prevent transport losses from the core to the edge. The start-up and ramp-up of this current have been commonly driven by a toroidal electric field induced by current changes in a center solenoid (CS) magnet. However, this causes engineering difficulties for the ST

* Authors to whom any correspondence should be addressed.

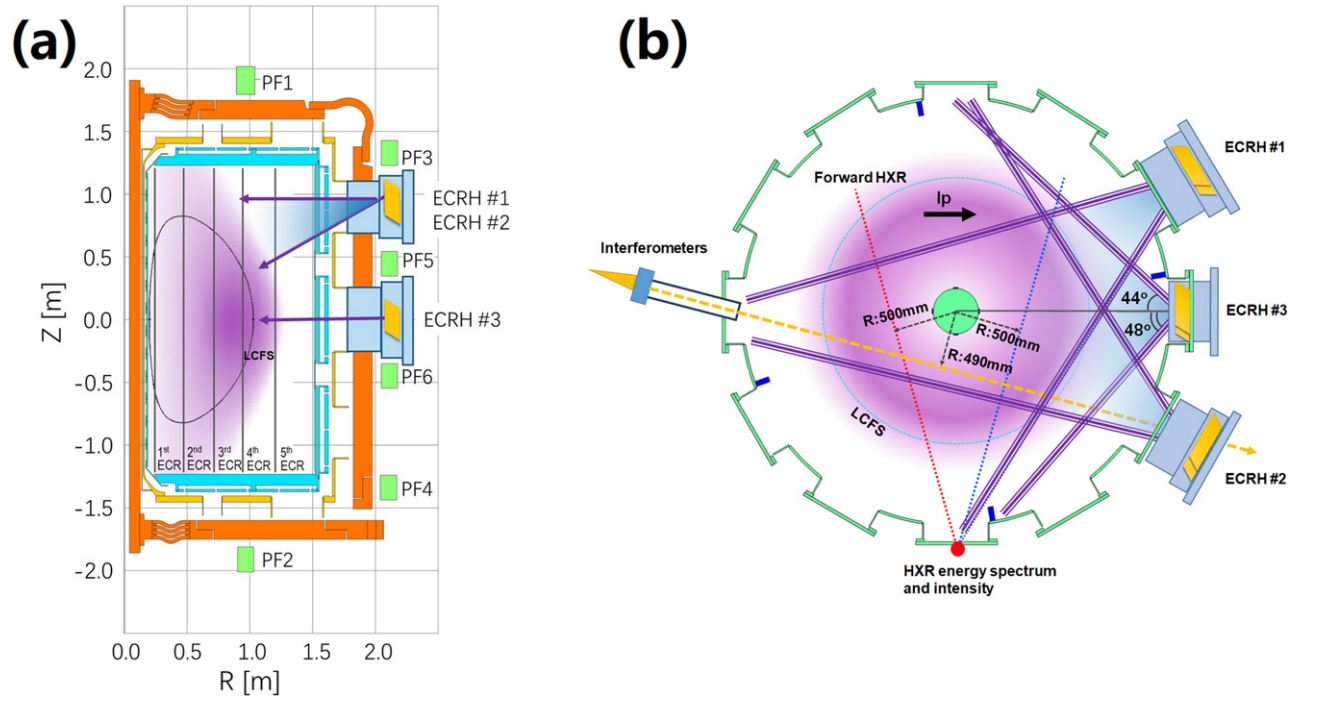

Figure 1. (*a*) Poloidal cross-section of the EXL-50 device. Nominal TF is 1 T at $R = 0.24$ m. (*b*) Top view of EXL-50. Lines of sight of the interferometer and HX diagnostics are indicated in the figure. ECRH beam is aimed at the center of the machine when the toroidal injection angles is 0°. Typical plasma cross-section (purple cloud) is also shown in figures 1(*a*) and (*b*).

due to the limited space available within a narrow center column. Furthermore, a CS magnet is capable of sustaining the plasma current over limited time period, which is to be augmented by non-inductive methods in a future fusion reactor. Therefore, to develop a solenoid-free current drive capability has been an important research endeavour for the STs. On the positive side, removing the CS allows additional space to increase the toroidal field (TF), further improving compactness and economy.

The original physics concept and principle of the ENN Spherical Torus with a major radius of 58 cm (EXL-50) in the Energy iNNovation (ENN) Science and Technology Development Co. were recently proposed by Martin Peng. One of the key EXL-50 experimental goals is to test the effectiveness of electron cyclotron resonance heating (ECRH) and current drive in the absence of a CS magnet. CS-free ECRH and current drive have been tested in several earlier ST devices (CDX-U [10], LATE [11–15], TST-2 [16, 17], MAST [18, 19] and QUEST [20–26]). A toroidal current of 1.05 kA was generated using about 8 kW of ECRH power on CDX-U [9], proving the possibility of current start-up by ECRH alone. Later, a 7 kA plasma current was generated by about 30 kW ECRH in LATE [11, 12]. A current flattop with a closed flux surface (CFS) plasma was sustained for 60 ms in LATE, proving the potential for steady-state ECRH and current drive of the ST plasmas. In MAST, a plasma current of 73 kA was produced by 60 kW ECRH power with the help of the unique grooved mirror-polarizer installed on the central rod [18]. In QUEST, a plasma current of 90 kA was obtained with about 200 kW ECRH power through combined first and second harmonic resonances [24].

In this paper, we present the latest ECRH experimental results from EXL-50. Not only are the operational parameters of CS-free current drive by ECRH significantly expanded, but some remarkable plasma behavior is also observed. Discharges with plasma currents substantially above 100 kA are routinely obtained in EXL-50, with the current flattop sustained for up to or beyond 2 s. Data of current drive efficiency higher than 1 A current per Watt of ECRH power issued from the gyrotrons, averaged over hundreds of discharges, have been accumulated. Plasma currents as high as 80–100 kA have been achieved at line-densities over 0.5×10^{19} m^{-2}.

This paper is organized as follows: an introduction to the experimental setup in EXL-50 is given in section 2. The high-efficiency current drive experimental results are described in section 3. Section 4 gives the discussion of energetic electrons and current drive mechanisms. High-density current drive experiments are presented in section 5. Conclusions and future plans are summarized in section 6.

2. Experimental setup

The EXL-50 device is a medium-sized ST with a cylindrical vacuum vessel (see, figure 1). An important characteristic of EXL-50 is that it does not have a central solenoid. Six poloidal field (PF) coils are located outside the vacuum vessel and the TF coil conductors. Inner limiters on the center column and outer limiters on the vessel wall have leading edges at 0.186 and 1.512 m in the major radius, respectively. The design of the large space of EXL-50's vacuum vessel is mainly for the confinement and accommodation of energetic electrons whose spatial distribution area is larger than that of thermal

plasmas. Two microwave frequencies have been utilized so far, 28 GHz from high-power gyrotrons for higher TF discharges and 2.45 GHz from low-power magnetrons for lower TF discharges and wall cleaning. Figure 1 shows the poloidal cross-section of the EXL-50 device. Two sets of 28 GHz gyrotrons (50 kW source power for ECRH1 and 400 kW for ECRH2) are available to inject power through two outboard ports above the mid-plane. Another 400 kW 28 GHz gyrotron (ECRH3) and two sets of 2.45 GHz magnetrons (30 kW source power each) are available to inject power through the mid-plane ports. The toroidal injection angles of the ECRH systems can be adjusted over limited ranges (as shown in figure 1(*b*)). Both the 2.45 and 28 GHz systems are arranged to inject primarily ordinary-mode (O-mode) wave in recent experiments on the EXL-50. When the electric current of a 12-turn TF coils per turn was set to about 100 kA, the fundamental and higher ECR layers (up to five resonances) coexist within the EXL-50 vacuum region (as shown in figure 1(*a*)). The electron density is measured using a single-chord tangential microwave interferometer [27]. Two CdTe detectors with energy resolution are applied to observe the forward and backward bremsstrahlung hard x-ray (HX) emission [28].

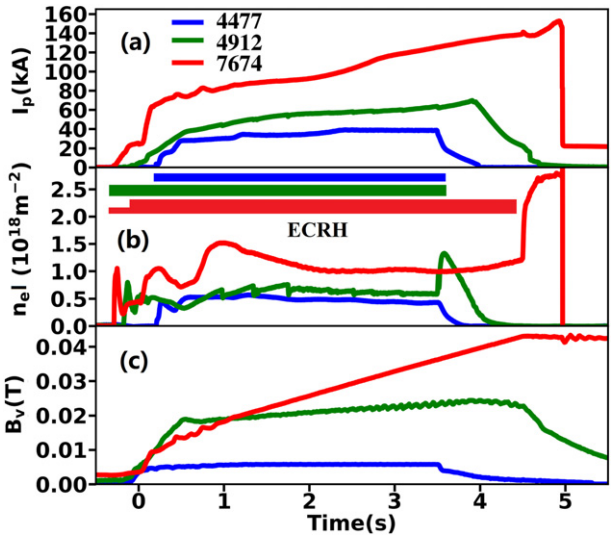

Figure 2. Discharge waveforms for different 28 GHz ECRH heating power. (*a*) Plasma current; (*b*) line integrated density; (*c*) external vertical magnetic field at $R = 0.5$ m in the mid-plane. P_{ECRH} was 20 kW in shot 4477 and 45 kW in shot 4912, respectively. Two gyrotrons are used in shot 7674. One gyrotron injected 20 kW from −0.3 to 0 s and the other gyrotron injected 115 kW from 0 to 4.5 s.

3. High-efficiency current drive experimental results in EXL-50

Here, a simplified current drive effectiveness $\eta_{\mathrm{A/W}}$ is defined as follows and utilized:

$$\eta_{\mathrm{A/W}} = I_{\mathrm{p}}/P_{\mathrm{ECRH}},$$

where I_{p} is the plasma current and P_{ECRH} is the ECRH power issued from the gyrotrons. Figure 2 shows the typical discharge waveforms with different 28 GHz ECRH heating power in EXL-50. The $\eta_{\mathrm{A/W}}$ can reach 2 A/W (40 kA/20 kW) for low ECRH power plasma. The $\eta_{\mathrm{A/W}}$ is 1.55 A/W (70 kA/45 kW) for moderate ECRH power plasma and 1.22 A/W (140 kA/115 kW) for further increased ECRH power plasma. The major and minor radii during the flattop phase for the thermal plasma inside the last closed magnetic surface are 0.59 and 0.41 m for shot 4477, 0.44 and 0.26 m for shot 4912, and 0.52 and 0.34 m for shot 7674, respectively. The line-averaged density during the flattop phase is around 0.26×10^{18} m^{-3}, 0.61×10^{18} m^{-3} and 0.80×10^{18} m^{-3}, respectively, for the three shots in figure 2. The P_{ECRH} in this paper is the power measured at the matching optical unit, which is close to the exit power of the gyrotrons. The power delivered from the antenna inside the vacuum vessel is unknown at present due to the lack of monitoring equipment. A directional coupler in the miter bend will be installed to obtain the waveform of the injected power in future experiments. The duration of high current ($I_{\mathrm{p}} > 100$ kA) for the higher ECRH power plasma in figure 2 is longer than 2 s. The total pulse length for 28 GHz ECRH heating plasma is less than 6 s. It is limited by temperature rise at the top joints of the TF coils at 100 kA current. One notable phenomenon shown in figure 2 is the density jump when the ECRH power is turned off, indicating a possible cessation of density pump-out by ECRH [29] or confinement transition, which is not addressed in this paper.

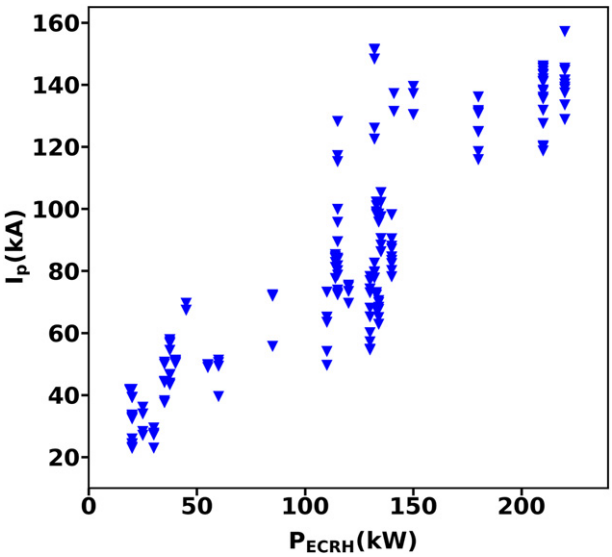

Figure 3. I_{p} versus P_{ECRH} for 200 successful shots in EXL-50.

Figure 3 shows the relation of I_{p} versus P_{ECRH} for about 200 successful shots in EXL-50. The general trend in figure 3 is that the I_{p} increases with P_{ECRH}. On the other hand, it can also be seen in figure 3 that the I_{p} varies in quite large range for the same P_{ECRH}. The uncertainty of actual injected and absorbed power by plasma may be one reason for the scattering relation between I_{p} and P_{ECRH} in figure 3. At the same time, changes of the currents in PF coils and the vertical magnetic field B_{v} have substantial effects on $\eta_{\mathrm{A/W}}$. For the same coil currents, B_{v} (at $R = 0.5$ in the mid-plane) contributed from PF5 and PF6 is around six times as high as that of PF1 and PF2, and twice as

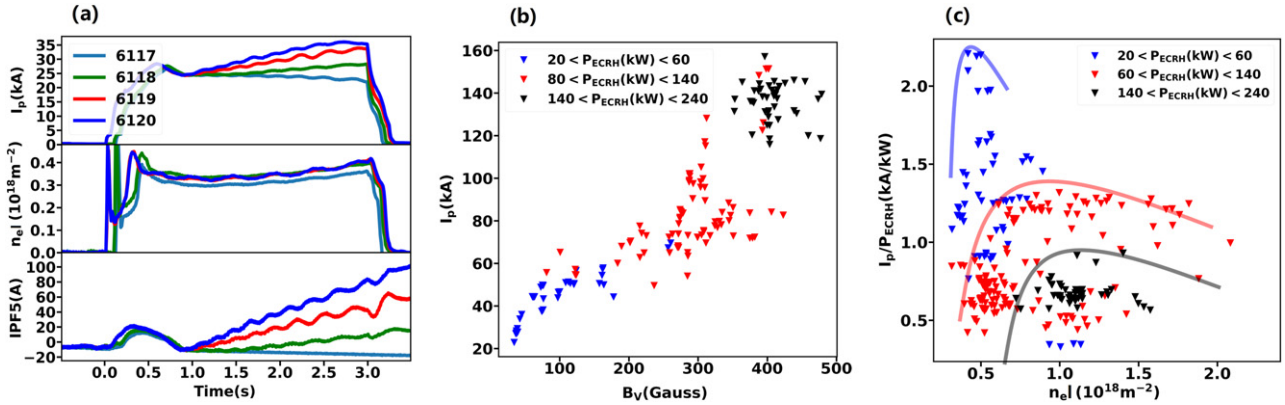

Figure 4. (*a*) Waveforms of four discharges with similar density. Waveforms from top to bottom are plasma current, line integrated density, and the electrical current in PF5 coil. P_{ECRH} was 25 kW for these shots. Current in PF1 and PF3 was kept constant ($I_{PF1} = 100$ A and $I_{PF3} = 600$ A) during the whole discharge phase. (*b*) Plasma current in the flattop phase versus external B_v at $R = 0.5$ m in mid-plane. (*c*) I_p/P_{ECRH} versus line integrated density.

high as that from PF3 and PF4. Thus, we have performed special discharge experiments, as shown in figure 4(*a*). In these discharges, only the current in PF5 and PF6 are changed to show the effect of B_v on plasma current, while the other parameters are the same in order to show the effect of B_v on plasma currents. Figure 4(*a*) clearly shows that the I_p increases with the current in PF5 and PF6 coils for the same P_{ECRH} and density. The force balance between the expansion of the plasma itself and external magnetic compression must be sustained for a stable equilibrium configuration. More statistical information from 200 shots is shown in figure 4(*b*). It is found that the I_p increases with the external vertical magnetic field B_v in the appropriate P_{ECRH} range. Figure 4(*b*) also demonstrates that both B_v and P_{ECRH} are essential elements for increasing the plasma current. B_v is not a plasma current driving source, but it will affect the maximum plasma current driven by ECRH. So much potential for raising $\eta_{A/W}$ through optimizing and matching of PF coil current and power of ECRH remains unexplored at present, which will be explored and improved in future experiments in EXL-50. In the first experimental campaign in EXL-50, the main target is to start-up and maintain plasma current. The density is operated in a narrow range ($0.5–2 \times 10^{18}$ m^{-2}) for the shots in figure 3. Figure 4(*c*) shows the relation between the plasma current and density in the flattop phase for the same shots in figures 3 and 4(*b*). It can be seen that too low density is not conducive to an increase in plasma current. The most suitable density for high I_p increases with P_{ECRH}.

4. Energetic electrons and current drive mechanisms

The Pfirsch–Schluter current is a dominant component during the initial start-up phase, and drastically decreases with increasing B_v following the formation of CFS. The bootstrap current drive by the pressure gradient is at present estimated to be less than several percent for these EXL-50 plasmas. The conventional electron cyclotron current drive

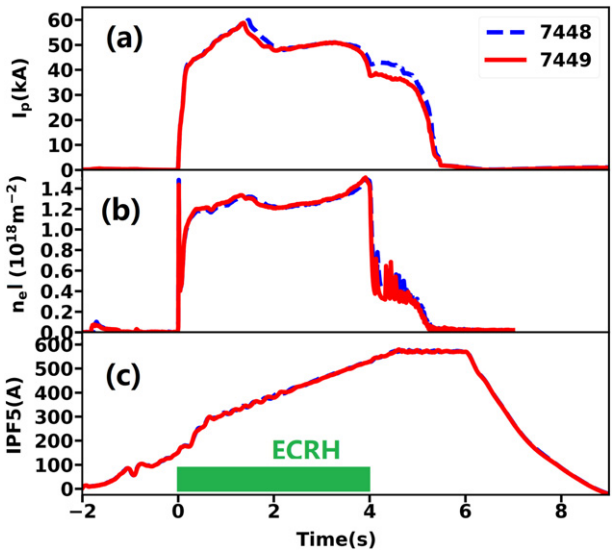

Figure 5. Waveforms of discharges with the same density, ECRH power and PF coil current. (*a*) Plasma current; (*b*) line-integrated density and (*c*) the current in PF5; the toroidal angle of ECRH antenna is in the co-current direction in shot 7448 and counter-current direction in shot 7449.

(ECCD) via Fisch–Boozer mechanism [30] or Ohkawa mechanism [31] can also contribute to the non-inductive current. However, these ECCD effects, being sensitive to the ECRH injection angle, have not been confirmed in EXL-50 experiments. Figure 5 shows the waveforms of two shots with the same P_{ECRH} in EXL-50. Although the toroidal angle for the ECRH antenna was set at -16° for counter-current drive in shot 7448 and 17° for co-current drive in shot 7449, the plasma current remained largely unchanged. The single-pass absorption of electron cyclotron wave (ECW) is very weak in the present low-temperature EXL-50 plasmas. The angle and mode of ECW are randomized during the multiple wall reflections, so that the conventional ECCD mechanism may contribute a negligible fraction to the total plasma current.

QUEST and LATE experiments have proved that the energetic electrons play a primary role in the CS-free current drive.

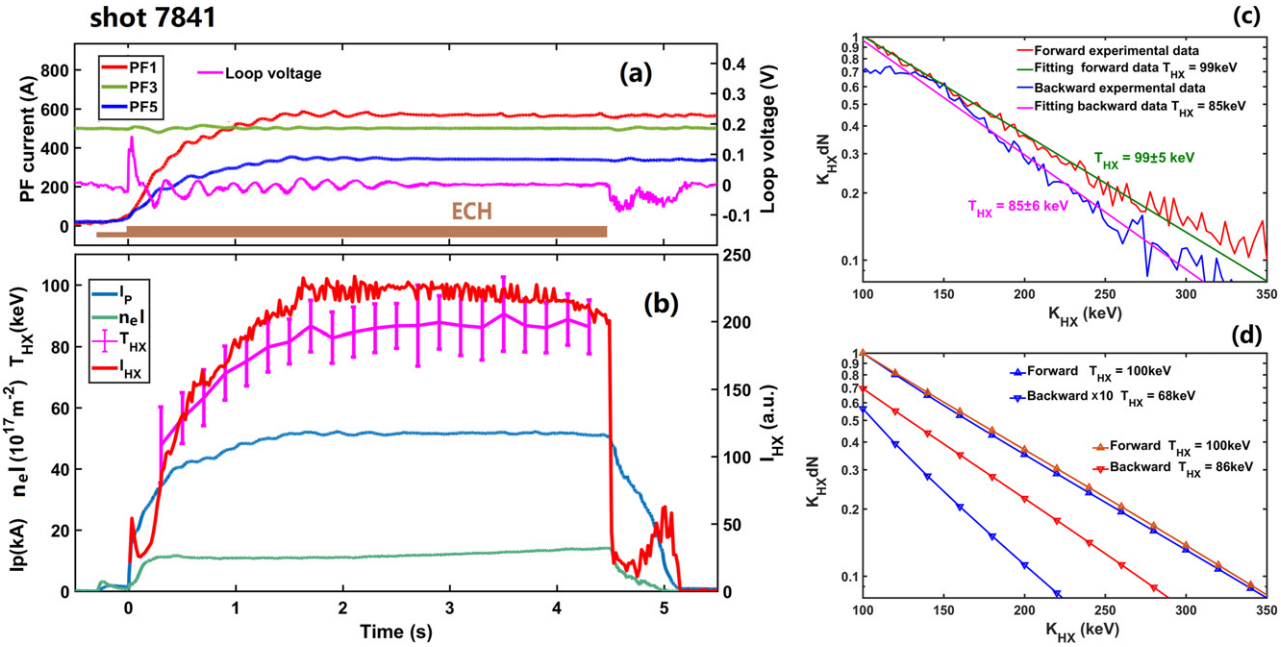

Figure 6. (*a*) Waveforms of PF currents (PF1, PF3 and PF5), loop voltage and ECRH. (*b*) Waveforms of plasma current (I_p), density (n_e), temperature (THX) and intensity (IHX) of HX. One gyrotron injected 10 kW from −0.3 to 0 s and the other gyrotron injected 100 kW from 0 to 4.5 s. (*c*) HX spectrum (integrated time: 2–2.2 s) in the forward and backward direction during the flattop phase. Data are normalized with intensity with the intensity at 100 keV of forward HX. (*d*) Simulated HX spectrum with a three-temperature distribution model for energetic electrons. Blue line (runaway case): $T_{\|F} = 10T_{\perp} = 10T_{\|B}$. Backward data are magnified ten times. Data are normalized with intensity at 100 keV of forward HX. Red line: $T_{\|F} = T_{\perp}$, $T_{\|B} = 0.75T_{\|F}$. Data are normalized with intensity at 100 keV of forward HX.

EXL-50 experimental results confirm that the plasma current is mainly carried by these energetic electrons. The shot shown in figure 6 is a very stable and well-controlled discharge, showing a nearly stationary plasma current, electron density, as well as a zero loop voltage from 1.5–4.5 s. During the entire discharge, the plasma current, HX intensity and its photon temperature (the average energy of energetic electrons) vary conjointly in magnitude. It can be seen that both the number and energy of energetic electrons contribute directly to the increase in plasma current.

It should be noted that the role of induction in the CS-free ECRH-driven current remains unresolved. That is, does the toroidal electric field induced by changes in the PF coils and plasma currents accelerate the already decoupled energetic electrons to even higher energies and carry a significant fraction of plasma current during a discharge? Experiments dedicated to resolving this question were carried out. As indicated in figure 6(*a*), the currents in PF3 and PF4 (not indicated) were kept constant during the entire discharge. The currents of PF1 and PF2, and PF5 and PF6 were ramped-up slowly until 1.5 s and kept constant through to 6 s. The loop voltage oscillated near zero between 1.5–2.5 s and became zero between 2.5–4.5 s. The loop voltage, measured at the mid-plane of the low-field side, is the main source for driving inductive plasma current. The definition of polarity for loop voltage and I_p in EXL50 is the reverse of each other. A positive loop voltage means counter-clockwise direction from the top view. A positive I_p means clockwise direction from the top view. The largest value of loop voltage of +0.17 V appears at 0.037 s, in the direction opposite to the plasma current. Therefore, the contribution to the inductive plasma current from loop voltage has a negligible or even negative contribution to the total plasma current during the start-up and flattop phases. In addition, the velocity distribution of energetic electrons driven by ECRH is different to that of runaway electrons induced by a toroidal electric field. In the former case, the energetic electrons possess similar magnitudes of parallel and perpendicular velocities, while in the latter, the parallel velocities dominate. Figure 6(*c*) shows the HX intensity and energy spectrum in the forward (counter-current) and backward (co-current) direction, indicating relatively moderate differences. The three-temperature Maxwellian distribution model (3T model) [32, 33] can be applied for the anisotropic distribution of runaway electrons or energetic electrons in RF heating plasmas. The detail for the HX spectrum simulation is presented in appendix A. The simulated HX spectrum based on the 3T model is shown in figure 6(*d*). In the runaway distribution case ($T_{\|F} = 10T_{\perp} = 10T_{\|B}$, blue line in figure 6(*d*)), the simulated backward HX intensity at 100 keV is around 1/20 that of forward HX intensity. The backward photon temperature of HX is only 2/3 that of forward HX in the runaway cases. Compared to the runaway simulation cases, the simulated HX spectrum based on the distribution of equal parallel forward and perpendicular temperature (red line in figure 6(*d*)) is much more approximate to the experimental data in figure 6(*c*). On the other hand, the energetic electrons can be strongly accelerated in the parallel direction by the relative high loop voltage during

current ramp-down after the ECRH is turned off. These experimental observations indicate that inductive and runaway-like current drive mechanisms are not significant in CS-free ECRH plasmas.

A key question regarding the very high current drive effectiveness ($\eta_{A/W} = 1.2–2$ A/W) in EXL-50 via the energetic electrons may be addressed by analyzing the asymmetric region of orbit containment of the energetic electrons. Figure 7 shows the orbit confinement analysis for energetic electrons in velocity space. A three-fluid equilibrium of a 50 kA EXL-50 plasma was obtained via the multi-fluid equilibrium model [33] for the computation of the guiding-center orbits [34]. A strongly asymmetric distribution in the parallel direction of the contained orbits in the $v_{\|}$, $v_{\perp}$ and energy space is obtained, and shown to be accentuated as the electron energy increases towards the limiting energy of orbit containment. The asymmetric structure of the confined energetic electron orbits, as shown in figure 7, is determined by the PF coil currents, not the ECRH injected angle. The population of energetic electrons is mainly related to the density and power of ECRH. As mentioned above, the conventional ECCD mechanisms provide a minor contribution to the total plasma current in EXL-50. Although the ECRH injection angles are quite different in the shots in figure 5, the plasma currents are quite similar because the other main parameters, such as the PF setting, density and ECRH power, are the same. Furthermore, the design of EXL-50 (as shown in figure 1(*a*)) permits the coexistence of five ECR layers within the vacuum vessel. Considering the effect of relativistic Doppler shift [23], the resonance layers for energetic electrons broaden in the major radius direction. Figure 8(*a*) shows the radial dependence of the characteristic resonant energies for the fundamental and harmonic ECW for EXL-50. For electrons of energy above 100 keV, the width of a resonance upshifts to overlap with the downshifted resonance of the next higher harmonic. It can be seen that the individual resonance widths for the energetic electrons fill the entire space inside EXL-50's vacuum vessel.

The single-pass absorption of ECW is estimated to be relatively low in EXL-50 for the present range of plasma densities and temperatures. The smooth stainless-steel vacuum vessel walls and limiters, including those on the center column, assist in ensuring multiple reflecting paths of the injected ECW back to the plasma. Wall-reflection further helps by converting O-mode wave to the X-mode and vice versa, thus taking advantage of the higher efficiency of X-modes by energetic electrons [26]. Another notable feature of EXL-50 plasma is that the cross-section of the plasma current carried by the energetic electrons is much bigger than that of the CFS during the flattop phase of plasma current. Figures 8(*b*) and (*c*) show 2D contour plots of plasma current, LCFS, and the profiles of thermal plasma and current for a 120 kA discharge shown in figure 2, computed via the multi-fluid equilibrium model [30]. A significant fraction of the plasma current (52% in this case) is flowing outside the LCFS. The phenomenon that the energetic electrons play a substantial role in the formation of CFS and carry a dominant fraction of the plasma current that extends over the open field line region in the solenoid-free ECRH sustained ST plasmas has been confirmed in LATE [11, 12]. Similar analysis has also been conducted in EXL-50. As a first approximation, a multi-fluid equilibrium model that includes a high-energy electron component in addition to the low-energy electron and ion components was applied to describe the equilibrium characteristics of EXL-50. The simulation results were in good agreement with the available experimental data [33]. Some special experiments have been performed in EXL-50 to indicate the considerable population of energetic electrons outside the LCSF [35]. Moreover, a removable limiter will be installed in a future machine upgrade plan. The space for a high harmonic ECH resonance layer and gap between the LCFS and limiter will be actively controlled to systematically investigate their effects on plasma current in EXL-50.

5. Current drive in high-density plasmas in EXL-50

High-density ECRH discharges are also obtained in EXL-50. The electron Bernstein wave (EBW) can be excited and played key role to heat plasma and drive current for the over-dense (i.e. the density is higher than the cut-off density of ECW) ECRH plasmas. This over-dense plasma has been achieved in the low TF (TF = 20 kA) operation mode in EXL-50. The 2.45 GHz microwave system is applied for the ECRH heating when the current of the TF coil is reduced to 20 kA. There are still two resonance layers that coexist for the 2.45 GHz ECRH in the low TF situation. The major radius for the three resonance layers are 0.55 and 1.1 m for the first and second harmonic, respectively. The typical discharge waveforms of over-dense plasma with 2.45 GHz ECRH heating are shown in figure 9(*a*). The line-averaged density can be as high as three times the ordinary mode (O-mode) cut-off density in the 2.45 GHz ECH discharges.

High-density plasma is obtained with multi-pulse gas puffing in 28 GHz ECRH discharges. The nozzle for gas puffing is located at the middle of the central stack ($Z = 0$ in figure 1(*a*)). It can be seen in figure 10 that the density increases rapidly at around 3 s. The plasma density retains high-level ($>5 \times 10^{18}$ m^{-2}) status from 3 to 4 s. At the same time, the plasma current is higher than 80 kA during the high-density phase. The density profile for core plasma is unavailable in EXL-50 at present. The core density may exceed the cut-off density of 28 GHz ECW in the high-density plasma. It is surmised that the EBW has been excited to drive current for such high-density discharges.

The general current drive efficiency $\eta_{CD} = n_e R I_p / P_{ECRH}$ for non-inductive current is estimated for the high-density ECRH experiments in EXL-50. For the 2.45 GHz ECRH high-density discharge in figure 9, $\eta_{CD} = n_e R I_p / P_{ECRH} = 0.013 \times 1019 \times 0.53 \times 3$ kA/20 kW is around 0.011×10^{19} MA MW m^{-2}. The $\eta_{CD} = n_e R I_p / P_{ECRH} = 0.43 \times 1019 \times 0.52 \times 85$ kA/150 kW is around 0.13×10^{19} MA MW m^{-2} for the 28 GHz ECRH high-density plasma in figure 10. High TF or ECRH frequency has tremendous benefit to improve the current drive efficiency. Here, we make a simple and initial estimation for the ECRH

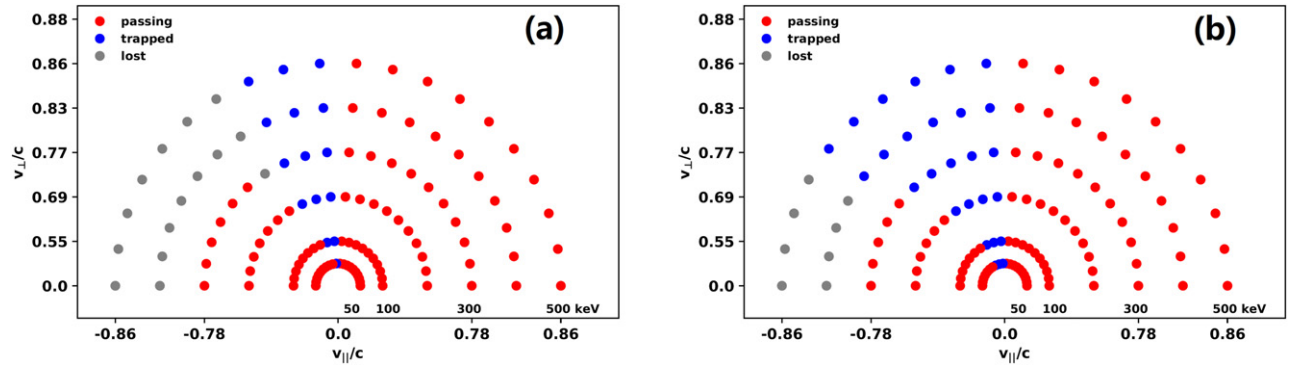

Figure 7. (*a*) Velocity distribution of energetic electrons, which start from the first harmonica layer at the mid-plane. (*b*) Velocity distribution of energetic electrons, which start from the magnetic axis. Background magnetic field for the simulation of energetic electrons is obtained from the three-fluid equilibrium model. Typical three-fluid equilibrium structure can be seen in figure 8.

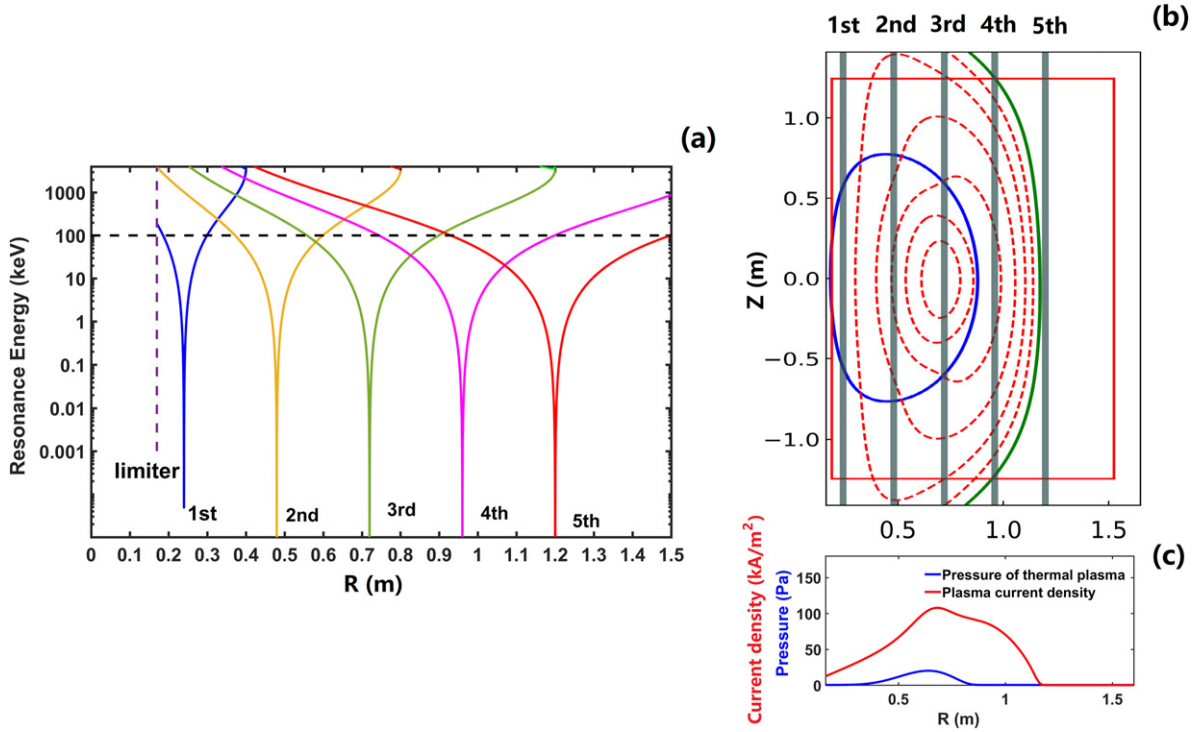

Figure 8. (*a*) Radial profiles of resonance energy for the harmonic ECW. (*b*) Reconstructed 2D contour plot of plasma current using the multi-fluid equilibrium model. Blue line represents the last closed flux surface (LCFS). (*c*) Radial profiles of thermal plasma pressure and current density.

current drive efficiency in STs based on the EXL-50's experimental results. We assume that the $\eta_{\rm CD}$ of ECRH in EXL-50-like STs has strong correlation with the wave frequency $f_{\rm ECRH}$ or toroidal magnetic field $B_{\rm T}$, i.e.,

$$\eta_{\rm CD} \propto f_{\rm ECRH}^{\alpha}, \quad \text{or } \eta_{\rm CD} \propto B_{\rm T}^{\beta}.$$

On the other hand, the ECRH frequency should match the TF. Based on the two sets of high-density experimental results on EXL-50, the indexes α and β in the above formula are estimated to be around 1.0 and 1.5, respectively. Although the experimental results show that the ECRH frequency or magnetic field has a strong effect on the current drive efficiency, the underlying physics mechanism needs to be investigated with some modelling and simulation tools in future research. ECRH is a promising tool for CS-free plasma current startup and sustainment in future ST reactors using higher-frequency ECRH at higher magnetic fields.

6. Summary

Current drive effectiveness and plasma current have reached new records in the CS-free ECRH experiments on EXL-50. The averaged current drive effectiveness on EXL-50 is around 1 A/W, which is around twice that (0.5 A/W) of previous similar experiments [19]. The plasma current routinely researches 150 kA, which is also higher than the

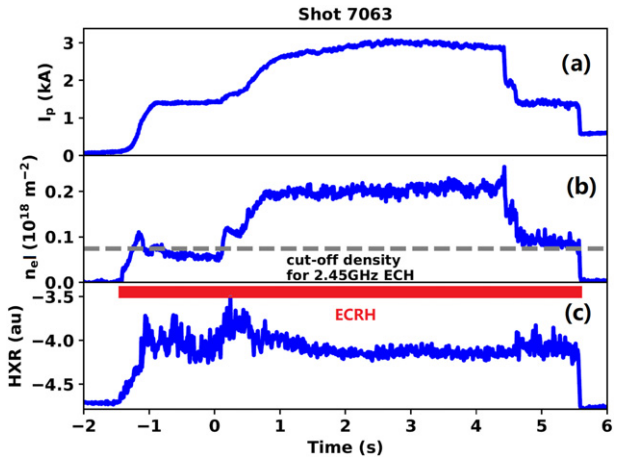

Figure 9. Waveforms of high-density discharge with 2.45 GHz ECRH. P_{ECRH} was 20 kW. Waveforms from top to bottom are (*a*) plasma current, I_{p}; (*b*) line-integrated density; (*c*) intensity of HX.

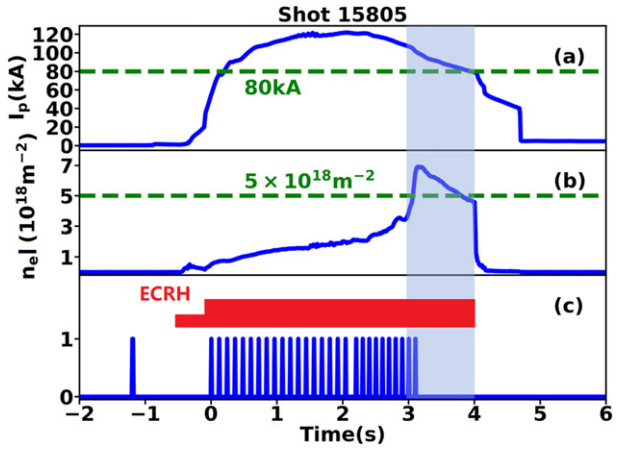

Figure 10. Waveforms of high-density discharge with 28 GHz ECRH. P_{ECRH} was about 150 kW. Waveforms from top to bottom are: (*a*) plasma current I_{p}; (*b*) line integrated density; (*c*) control signal of gas-puffing. One gyrotron injected 20 kW from −0.5 to 1.5 s and the other gyrotron injected 150 kW from −0.1 to 4 s.

maximum value (∼90 kA) of a previous CS-free ECRH experiment [24]. The energetic electrons play a unique and important role in EXL-50's plasmas. The metal wall of the vacuum vessel effecting multiple reflections and absorption at high multi-harmonic resonances increases the high efficiency of acceleration of the energetic electrons. The asymmetric distribution of the energetic electrons in velocity space based on orbit analysis in a multi-fluid equilibrium is another key feature of the very high current drive effectiveness observed. However, the physics mechanism for the solenoid-free ECRH current drive is not yet well understood and quantifiable. Nevertheless, these results demonstrate the exceptional potential of ECRH to achieve and maintain highly efficient steady-state current drive over a density range up the ECRH cut-off density in the CS-free EXL-50 device. Theory, modelling and simulation to better describe the full range of mechanisms associated with the CS-free current drive observed will be systematically developed in the upcoming research. Steady-state high current and density experiments using high ECRH power on EXL-50 will make physics contributions of an efficient current drive method for use in an eventual commercial ST fusion reactor.

Acknowledgments

Y.J. Shi gratefully acknowledges Dr Houyang Guo (ENN), Dr Huasheng Xie (ENN) and Prof. Jiaqi Dong (SWIP) for their assistance in carefully reading the manuscript and commenting on it.

Appendix A. Simulation of HX spectrum based on a three-temperature distribution model for energetic electrons

The anisotropic velocity distribution function f_{s} of the superthermal electrons in magnetic confined plasma can be represented by a three-temperature Maxwellian model (3T model) [32]:

$$f_{\mathrm{s}}(\vec{p}) = C_{\mathrm{N}} \exp\left(-\frac{p_{\perp}^2}{2T_{\perp}} - \frac{p_{\parallel}^2}{2T_{\parallel \mathrm{F}}}\right) \quad \text{for } p_{\parallel} \geqslant 0$$

$$f_{\mathrm{s}}(\vec{p}) = C_{\mathrm{N}} \exp\left(-\frac{p_{\perp}^2}{2T_{\perp}} - \frac{p_{\parallel}^2}{2T_{\parallel \mathrm{B}}}\right) \quad \text{for } p_{\parallel} < 0$$

$$\text{and} \quad f_{\mathrm{s}}(\vec{p}) = 0, \quad \text{for } \vec{p} > p_{\mathrm{c}},$$

where $p_{\parallel}$ and $p_{\perp}$ are the parallel and perpendicular components of the momentum with respect to the magnetic field, normalized to the electron rest momentum $m_{\mathrm{e}}c$; $T_{\perp}$, while $T_{\parallel \mathrm{F}}$ and $T_{\parallel \mathrm{B}}$ are the perpendicular, parallel forward and parallel backward temperature, respectively, normalized to the electron rest mass $m_{\mathrm{e}}c^2$; p_{c} is the upper cut-off momentum ($p_{\mathrm{c}} = \sqrt{\left(10T_{\parallel \mathrm{F}} + 1\right)^2 - 1}$ in simulation). For the runaway electrons, the perpendicular and parallel backward velocities are much smaller than the parallel forward velocity. Thus, $T_{\parallel \mathrm{F}} \gg T_{\perp}$ and $T_{\parallel \mathrm{B}}$ in 3T model can represent the distribution of runaway electrons. For the energetic electrons generated by RF heating, the perpendicular and parallel backward velocities are the same order as the parallel forward velocity. $T_{\parallel \mathrm{F}} \sim T_{\perp}$ and $T_{\parallel \mathrm{B}}$ in the 3T model is a good approximation for the distribution of energetic electrons in RF plasma.

Only the electron–ion bremsstrahlung radiation is considered for the HX simulation. The electron–electron bremsstrahlung and recombination radiation can be neglected compared to the electron–ion bremsstrahlung [32]. The x-ray is the line-integrated measurement. The radial profile of ion density, energetic electron density and temperatures in the 3T model are the key parameters to determine the shape of the HX spectrum. For the simulation of the HX spectrum in EXL-50, the energetic electron density is assumed to be constant in the thermal plasma region. The profiles of the ion density and energetic electron temperatures are assumed to be parabolic distribution. $T_{\perp}/T_{\parallel \mathrm{F}}$ and $T_{\parallel \mathrm{B}}/T_{\parallel \mathrm{F}}$ are 0.1 and 0.1 for the runaway case, and 1 and 0.75 for the ECRH case,

respectively. The ratio of $T_{\perp}/T_{\|\mathrm{F}}$ and $T_{\|\mathrm{B}}/T_{\|\mathrm{F}}$ is fixed and does not change with radius. Under the above assumption, the best fitting of forward HX spectrum for 7841 in figure 6 can be obtained when the peak value of $T_{\|\mathrm{F}}$ is set as 220 keV for the runaway case and 180 keV for the ECRH case.

Appendix B. The EXL-50 Team

Minsheng Liu, Y-K Martin Peng, Baoshan Yuan, Yuejiang Shi, XianMing Song, Bing Liu, Shaodong Song, Xin Zhao, Enwu Yang, Wenwu Luo, Peihai Zhou, Yuanming Yang, Bo Xin, Yunyang Song, Dong Guo, Jiaqi Dong, Huasheng Xie, Yubao Zhu, Wenjun Liu, Xiang Gu, Di Luo, Bin Chen, Tiantian Sun, Zhi Li, Mingyuan Wang, Hanyue Zhao, Yukun Bai, Haojie Ma, Debabrata Banerjee, Akio Ishida, Takashi Maekawa, Xiaorang Tian, Chao Wu, Guosong Zhang, Shunqiao Huang, Hao Li, Zimo Gao, Jiangbo Ding, Qing Zhou, He Liu, Lei Han, Pengmin Li, Hanqing Wang, Zhenxing Wang, Yupeng Guan, Zhen Li, Zihua Kang, Yong Liu, Xiuchun Lun, Dongkai Qi, Wei Wang, Quan Wu, Chunqi Liu, Kun Han, Yu Wang, Bo Chen, Renhua Bai, Xiaokun Bo, Pengmei Jia, Hong Zang, Yunfeng Gu, Jianbo Hao, Hefei Yuan, Xu Yang, Xiang Gao, Lianxing Chen, Shaoxun Liu, Yumin Wang, Yingying Li, Shikui Cheng, Xianli Huang, Songjian Li, Xiaomin Tian, Renyi Tao, Hongyue Li, Bihe Deng, Qifeng Xie, Jiahe Liu, Chunrong Feng, Lingling Dai, Weiqiang Tan, Lin Chen, Ji Qi, Lihua Chen, Wenhao Cui, Shuo Wang, Song Liu, Haiwei Zhao, Afeng Zhao, Wei Yuan, Haiwei Zhao, Cece Dong, Fei Liu, Jun Zhao, Wenyin Li, Zequn Sun, Jianbo Hou, Huiling Wang, Chen Bian, Qinhai Wang, Xinxin Ma, Weigang Li, Jinmeng Dong, Jun Tan, Zeying Du, Kaiming Feng, Houyang Guo, Zhenqi Zhu

ORCID iDs

Yuejiang Shi https://orcid.org/0000-0002-9572-3310
Dong Guo https://orcid.org/0000-0001-6562-8841
Yingying Li https://orcid.org/0000-0002-2978-908X
Debabrata Banerjee https://orcid.org/0000-0002-7882-6369
Takashi Maekawa https://orcid.org/0000-0001-6837-8219

References

[1] Artsimovich L.A. *et al* 1968 *Proc. 3rd Int. Conf. Novosibirsk* (Novosibirsk) vol 1 (Vienna: IAEA) p 157 (http://naweb.iaea.org/napc/physics/FEC/STIPUB192_VOL1.pdf)
[2] Artsimovich L.A., Bobrovskii G.A., Mirnov S.V., Razumova K.A. and Strelkov V.S. 1967 Thermal insulation of plasma in the tokamaks? *Sov. At. Energy* **22** 325–31
[3] Peacock N.J., Robinson D.C., Forrest M.J., Wilcock P.D. and Sannikov V.V. 1969 Measurement of the electron temperature by Thomson scattering in tokamak T3 *Nature* **224** 488–90
[4] Peng Y.-K.M. and Strickler D.J. 1986 Features of spherical torus plasmas *Nucl. Fusion* **26** 769–77
[5] Peng Y.-K.M. 2000 The physics of spherical torus plasmas *Phys. Plasmas* **7** 1681–92
[6] Sykes A. *et al* 1997 High-performance of the START spherical tokamak *Plasma Phys. Control. Fusion* **39** B247–60
[7] Synakowski E.J. *et al* 2003 The national spherical torus experiment (NSTX) research programme and progress towards high beta, long pulse operating scenarios *Nucl. Fusion* **43** 1653–64
[8] Buttery R.J. *et al* 2004 Stability at high performance in the MAST spherical tokamak *Nucl. Fusion* **44** 1027–35
[9] Gusev V.K. *et al* 2009 Overview of results obtained at the Globus-M spherical tokamak *Nucl. Fusion* **49** 104021
[10] Forest C.B., Hwang Y.S., Ono M. and Darrow D.S. 1992 Internally generated currents in a small-aspect-ratio tokamak geometry *Phys. Rev. Lett.* **68** 3559–62
[11] Maekawa T. *et al* 2005 Formation of spherical tokamak equilibria by ECH in the LATE device *Nucl. Fusion* **45** 1439–45
[12] Yoshinaga T., Uchida M., Tanaka H. and Maekawa T. 2006 Spontaneous formation of closed-field torus equilibrium via current jump observed in an electron-cyclotron-heated plasma *Phys. Rev. Lett.* **96** 125005
[13] Uchida M., Yoshinaga T., Tanaka H. and Maekawa T. 2010 Rapid current ramp-up by cyclotron-driving electrons beyond runaway velocity *Phys. Rev. Lett.* **104** 065001
[14] Kuroda K., Wada M., Uchida M., Tanaka H. and Maekawa T. 2016 Shift in principal equilibrium current from a vertical to a toroidal one towards the initiation of a closed flux surface in ECR plasmas in the LATE device *Plasma Phys. Control. Fusion* **58** 025013
[15] Tanaka H. 2018 Electron Bernstein wave heating and current drive with multi-electron cyclotron resonances during non-inductive start-up on LATE *2018 IAEA Fusion Energy Conf.* (Gandhinagar) EX/P3-19 (Ahmedabad, India) (https://nucleus.iaea.org/sites/fusionportal/Shared%20Documents/FEC%202018/fec2018-preprints/preprint0078.pdf)
[16] Ejiri A. *et al* 2009 Non-inductive plasma current start-up by EC and RF power in the TST-2 spherical tokamak *Nucl. Fusion* **49** 065010
[17] Takase Y. *et al* 2013 Non-inductive plasma initiation and plasma current ramp-up on the TST-2 spherical tokamak *Nucl. Fusion* **53** 063006
[18] Shevchenko V.F., O'Brien M.R., Taylor D. and Saveliev A.N. 2010 Electron Bernstein wave assisted plasma current start-up in MAST *Nucl. Fusion* **50** 022004
[19] Shevchenko V.F. *et al* 2015 Long pulse EBW start-up experiments in MAST *EPJ Web Conf.* **87** 02007
[20] Hanada K. *et al* 2011 Non-inductive start up of QUEST plasma by RF power *Plasma Sci. Technol.* **13** 307–11
[21] Ishiguro M. *et al* 2012 Non-inductive current start-up assisted by energetic electrons in Q-shu University experiment with steady-state spherical tokamak *Phys. Plasmas* **19** 062508
[22] Tashima S. *et al* 2014 Role of energetic electrons during current ramp-up and production of high poloidal beta plasma in non-inductive current drive on QUEST *Nucl. Fusion* **54** 023010
[23] Idei H. *et al* 2017 Fully non-inductive second harmonic electron cyclotron plasma ramp-up in the QUEST spherical tokamak *Nucl. Fusion* **57** 126045
[24] Idei H. *et al* 2018 Fully non-inductive 2nd harmonic electron cyclotron current ramp-up with polarized focusing-beam in the quest spherical tokamak *2018 IAEA Fusion Energy Conf.* (Gandhinagar) EX/P3-21 Ahmedabad, India) (https://nucleus.iaea.org/sites/fusionportal/Shared%20Documents/FEC%202018/fec2018-preprints/preprint0175.pdf)
[25] Idei H. *et al* 2020 Electron heating of over-dense plasma with dual-frequency electron cyclotron waves in fully non-inductive plasma ramp-up on the QUEST spherical tokamak *Nucl. Fusion* **60** 016030
[26] Onchi T. *et al* 2021 Non-inductive plasma current ramp-up through oblique injection of harmonic electron cyclotron waves on the QUEST spherical tokamak *Phys. Plasmas* **28** 022505

[27] Li S.J., Bai R.H., Tao R.Y., Li N., Lun X.C., Liu L.C., Liu Y., Liu M.S. and Deng B.H. 2021 A quasi-optical microwave interferometer for the XuanLong-50 experiment *J. Inst.* **16** T08011

[28] Cheng S.K., Zhu Y.B., Chen Z.Y., Li Y.X., Bai R.H., Chen B., Huang X.L., Dai L.L. and Liu M.S. 2021 Tangential hard x-ray diagnostic array on the EXL-50 spherical tokamak *Rev. Sci. Instrum.* **92** 043513

[29] Angioni C., Fable E., Greenwald M., Maslov M., Peeters A.G., Takenaga H. and Weisen H. 2009 Particle transport in tokamak plasmas, theory and experiment *Plasma Phys. Control. Fusion* **51** 124017

[30] Fisch N.J. and Boozer A.H. 1980 Creating an asymmetric plasma resistivity with waves *Phys. Rev. Lett.* **45** 720–2

[31] Ohkawa T. 1976 *Steady-State Operation of Tokamaks by rf Heating* (General Atomics) Report No. GA A13847

[32] Stevens J. *et al* 1985 Modelling of the electron distribution based on bremsstrahlung emission during lower-hybrid current drive on PLT *Nucl. Fusion* **25** 1529–41

[33] Ishida A., Peng Y.-K.M. and Liu W. 2021 Four-fluid axisymmetric plasma equilibrium model including relativistic electrons and computational method and results *Phys. Plasmas* **28** 032503

[34] Maekawa T., Yoshinaga T., Uchida M., Watanabe F. and Tanaka H. 2012 Open field equilibrium current and cross-field passing electrons as an initiator of a closed flux surface in EC-heated toroidal plasmas *Nucl. Fusion* **52** 083008

[35] Guo D. *et al* 2022 Experimental study of the characteristics of energetic electrons outside LCFS in EXL-50 spherical torus *Plasma Phys. Control. Fusion* **64** 055009